Deformation models and correlation analysis in elastography

Mehmet Bilgen and Michael F. Insana
Department of Radiology, University of Kansas Medical Center, Kansas City, Kansas 66160-7234

Cross-correlation functions are derived with the purpose of determining how strain inhomogeneities affect the displacement estimates used in ultrasound-based elastography. Variations in the strain profile occur in most imaging situations and are caused by fluctuations in the stress field or elastic modulus of the sample. An analytical framework for developing signal processing strategies in elastography is described, and the limitations of correlation-based methods for measuring displacements in tissuelike media caused by static compression are emphasized. This paper includes (1) an accurate approximation for an inverse coordinate transformation that relates pre- and postcompression reflectivity profiles of the media, (2) a derivation of the echo-signal cross-correlation function in media with deterministic or stochastic strain profiles; (3) mathematical and graphical descriptions of the consequences that nonuniformities in the strain profile impose upon the uncertainty of displacement estimation; and (4) a demonstration of the advantages of echo signal conditioning and ultrasonic-pulse shaping to reduce the nonstationary effects that attenuate the cross-correlation peak and reduce the signal-to-noise ratio for displacement estimation. © *1996 Acoustical Society of America.*

PACS numbers: 43.80.Cs, 43.80.Ev, 43.80.Qf

INTRODUCTION

Elastography is an application of the palpation principle that offers the possibility of increased sensitivity and spatial resolution for detecting changes in elastic properties deep in the body.[1] Physicians have long recognized the value of palpation as a diagnostic technique for detecting disease. During a physical examination, a physician's hand is used to apply a small force to the patient's skin surface while the finger tips sense for increases in tissue stiffness that could indicate the presence of a mass near the surface. Palpation is the basis of self-examination for detecting breast and testicular cancers. However, no current diagnostic test measures elasticity quantitatively.

Ultrasonic imaging of the breast is known to add new information to standard diagnostic procedures, such as x-ray mammography, and in some situations decreases the need for surgical biopsy.[2] For example, sonography can indicate whether a palpable mass is cystic or solid. This information is important for evaluating masses not visible in radiographically opaque breasts and other diagnostic situations. However, some solid lesions, such as invasive papillary carcinoma, are not visible with sonography.[2] It has been demonstrated in phantoms that *B*-mode images can fail to show solid inclusions positioned in a fluid background.[3] Therefore detection of low-contrast lesions may be improved by adding quantitative information about tissue elasticity.

In elastography, local tissue deformations produced by external compression are measured in order to describe the spatial distribution of elasticity. It is well known that ultrasonic echo signals can be used to measure tissue displacement and strain.[5–15] A common procedure is to cross correlate echo signals received before and after static compression. The maximum value of the cross-correlation function is used to locate the average displacement in that region. From displacement estimates, components of the strain tensor are computed and strain images are formed. With prior knowledge of the test medium, the calculated strain tensor may be substituted into the constitutive equations of continuum mechanics to reconstruct elastic modulus images.[16,17] The term ''elastogram'' can refer to either strain images or elastic modulus images. Elastic modulus images are preferred because they more accurately represent the intrinsic properties of the tissue and can maximize the inherent target contrast by reducing artifacts caused by stress nonuniformities.[16]

The elastic modulus that is calculated by straining the tissue is substantially different from the elastic modulus determined from the average wave speed in the medium. The former is a macroscopic feature of the material structure and the later is a microscopic feature of the structure. This difference has been observed in the solid mechanics of metals; the Young's modulus ($\sim 1800 \times 10^9$ dyne cm^{-2}) and shear modulus ($\sim 800 \times 10^9$ dyne cm^{-2}) among steels are nearly the same although the ultimate strengths vary a great deal depending on the crystalline structure.[18] While the elastic moduli of metals are ''structurally insensitive,'' the strengths are ''structurally sensitive.''

The ultimate goal of our effort is to maximize the low-contrast detectability of elastography for soft biological tissues. To achieve this goal, it is essential to understand how to adjust experimental parameters and signal processing variables to ensure a large sharp peak in the cross-correlation function, and thereby obtain accurate displacement estimates. This paper summarizes our analysis of echo-signal cross correlation that is the basis of elastographic image formation. We study how properties of the instruments and the tissue determine features of the cross-correlation function, and explain the advantages gained by processing signals before correlation. In particular, stretching the postcompression echo signal and/or shaping the ultrasonic pulse can signifi-
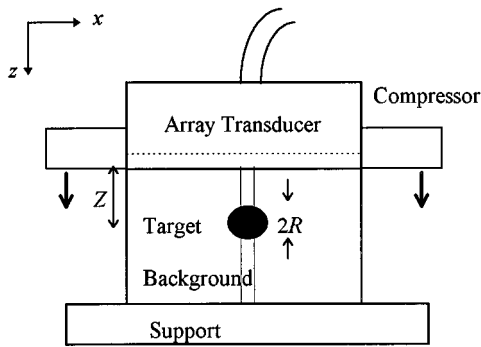
FIG. 1. Schematic geometry of an elastographic experiment.

FIG. 2. Illustration of precompression (top) and postcompression (bottom) slices.

cantly increase the magnitude of the cross-correlation function. Section I summarizes our assumptions regarding elastic properties of soft biological tissues and echo-signal formation that are essential to the description of tissue motion within the scan plane of the transducer. In Sec. II, we derive cross-correlation functions for tissuelike media that exhibit deterministic and stochastic strain profiles. In Sec. III, we discuss the results of the analysis by showing how modifications to the experiment and processing of the echo signals can reduce displacement errors. Finally, we conclude with a summary in Sec. IV.

I. BACKGROUND

A. Assumptions

Consider a uniaxial loading of an incompressible tissue sample along the z axis as defined by the axis of the ultrasound beam. Uniaxial loading will occur when the dimensions of coaxial, planar compressor plates are larger than the sample dimensions[19] as in Fig. 1, or when one compressor plate is smaller than the sample but appropriately shaped to produce a stress field that is constant in the x,y plane, varying only along z.[20] We also assume a plane-strain condition, where the strain is limited to the scan plane of the transducer, viz., the x,z plane of Fig. 1.

Cross-correlation of the two echo signals obtained before and after compression is considered. We assume the elastic properties of the material in the scan plane are isotropic but otherwise arbitrary. We also assume the elastic properties are constant in the direction perpendicular to the scan plane, along the y axis. In this two-dimensional (2-D) tissue model, the strain produced throughout the scan plane depends on the distribution of Young's modulus in the plane, $E(x,z)$, under the incompressibility condition. To study lesion detection, we now consider a sample in which the background medium is uniform, i.e., $E(x,z)=E_b$. Also, near the center of the sample at depth Z, there is an inclusion of dimension roughly $2R$ that is uniformly harder than the background material, i.e., $E(x,y)=E_0$, where $E_0>E_b$. We model the resulting strain profile in the scan plane as follows. Through the center of the inclusion, the strain profile along the z axis is essentially equivalent to that of the three layer problem diagrammed in Fig. 2. However, near the edge of the sample and far from the inclusion, the strain profile along the z axis is equivalent to that of a uniform sample containing background material, but with small fluctuations in the strain caused by the presence of the hard inclusion. The exact nature of the strain fluctuations will depend on the size, shape, and location of the inclusion. At positions along the x axis, between the center and edge of the sample, the strain profile is some combination of the above two models. Therefore, we begin modeling the 1-D axial correlation analysis of the 2-D strain profile by examining two simpler 1-D problems: the deterministic three-layer problem and the stochastic one-layer problem. Both are described in Section II.
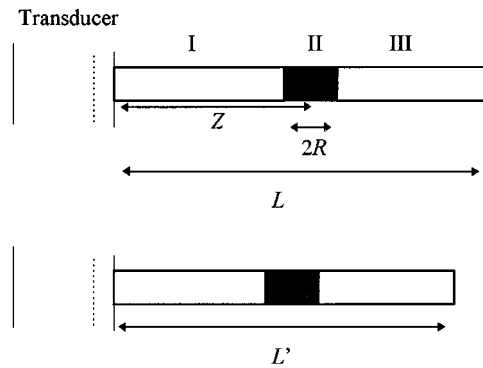
There is reason to assume that the large-scale elastic properties that determine the appearance of the elastogram are mostly uncoupled from the small-scale elastic properties that determine the appearance of the sonogram. To illustrate, consider the example of a cubic sample of incompressible soft tissue that is slowly compressed along the z axis. Slow compression is one way to ensure that the deformations are static and that only the elastic properties are important, i.e., viscous effects are negligible.[16] The stress T and strain s in the sample along the z direction are related via Hookes law:[21]

$$T_{zz}(z)=E(z)s_{zz}(z), \tag{1}$$

where $E\approx 3G$ is Young's modulus and G is the shear modulus. Equation (1) is valid only when the elasticity of the medium is isotropic. Since tissue is incompressible (Poisson's ratio ≈ 0.5) and responds linearly to the stress for small displacements, the lateral sides of the sample will bulge out in proportion to T_{zz}. Strains in the x and y directions are given by[21]

$$s_{xx}(z)=s_{yy}(z)=-T_{zz}(z)/2E(z). \tag{2}$$

Note that if the out-of-plane displacement of tissue along y is smaller than the corresponding dimension of the pulse-echo beam profile, then such motion can be ignored. Equations (1) and (2) indicate that the static deformations are completely characterized by features of the shear modulus since $E\approx 3G$.

Consider a second example in which the same tissue sample is now compressed by a force that varies sinusoidally in time, at ultrasonic frequencies (1–10 MHz). The sample responds to this force by propagating a compressional wave at the same frequency, but with an amplitude and wavelength that are determined by the bulk modulus (K) and longitudinal sound speed (c_l) of the sample.[22] Morse and Ingard (Ref. 23, p. 430) point out that scattering of the ultrasonic waves is

independent of G. They assert that, if spatial variations in G about the mean value are small and if their spatial extent (or correlation length for continuous random media) is larger than the ultrasonic wavelength, then fluctuations in the shear modulus do not interact with ultrasound waves. In support of this assertion, Sarvazyan[24] states that the ratio of shear wave intensity to longitudinal wave intensity I_s/I_l for comparable particle displacements in soft tissue is given by the ratio of shear to longitudinal sound speeds, $I_s/I_l = c_s/c_l$ and is small. Measurements by Madsen *et al.*[25] show that indeed $c_s/c_l \approx 10^{-2}$. In addition, the small amount of shear wave energy that is generated is then locally absorbed because the attenuation coefficient for shear waves is approximately 10^4 times that for longitudinal waves. The independence of elastographic and sonographic properties was also demonstrated in a contrast-detail phantom described by Hall *et al.* (Ref. 3, Fig. 5). Solid cylinders placed in a liquid background medium showed no sonographic contrast although differences between the elastic properties of the solids and liquid were great.

Independence is only possible if the shape of the acoustic scatterers is unmodified by the applied force. While the experimental evidence thus far suggests that such coupling between the strain and reflectivity profiles is small, it will decorrelate the pre- and postcompression echo signals if it exists, as we show below.

B. Echo signal formation

The geometry of a hypothetical elastographic measurement setup is shown in Fig. 1. An ultrasonic array transducer is mounted in a compressor plate placed in contact with a sample that is rigidly supported from below. The transducer transmits broadband pulses and receives echoes from weakly scattering structures. Microscopically, there are many random fluctuations in density and compressibility in the volume occupied by the pulse, producing a fully developed speckle pattern throughout the sample. Macroscopically, however, the sample is elastically uniform except for a hard inclusion at depth Z, similar to the isoechoic solid cylinders in the liquid background of the contrast-detail phantom described by Hall *et al.*[3] The microscopic variations in elasticity characterize the reflectivity profile, while the macroscopic variations determine the strain profile and consequently the axial scaling of the post-compression reflectivity profile.

The reflectivity profile at vector position $\mathbf{x}$ is represented by an isotropic scattering function $f(\mathbf{x})$. An echo signal $r(\mathbf{x},t)$ is formed by scanning the reflectivity profile with a transducer beam represented by the pulse-echo point spread function $h(\mathbf{x},t)$; both are functions of position and time. Mathematically, the echo signal is a three-dimensional convolution between the point spread function and the reflectivity profile.[26] However, for a stationary point spread function, the echo signal can be written as a 1-D convolution along the axis of the sound beam:[27]

$$r(z) = h \otimes f(z) + n(z), \tag{3}$$

where z is the axial distance from the transducer-compressor to the field point and related to the time of flight via $z =$ time $\times$ velocity/2. The sign $\otimes$ denotes convolution and the func-

tion $n(z)$ represents a signal-independent, zero-mean, spatially uncorrelated noise process, e.g., electronic noise.

In elastography, echo signals are acquired in pairs; the precompression signal and postcompression signal are distinguished by assigning an index of 1 and 2 to the associated variables, i.e.,

$$r_1(z) = h_1 \otimes f_1(z) + n_1(z)$$

$$\text{for the precompression signal} \tag{4}$$

and

$$r_2(z) = h_2 \otimes f_2(z) + n_2(z)$$

$$\text{for the postcompression signal.} \tag{5}$$

In the following, it will be explained why we also distinguished the point spread functions before and after the compression. The waveform segments r_1 and r_2 are compared using cross correlation. The location of the cross-correlation peak is employed to estimate the local displacement.

We model the pulse-echo point-spread function of the imaging system $h(z)$ as a Gaussian-modulated sinusoid with center (spatial) frequency $k_0 = 2\pi/\lambda_0$, where λ_0 is the wavelength and L_h is the correlation length that determine the pulse duration:

$$h(z,k_0,L_h) = \frac{1}{\sqrt{2\pi}L_h} \exp(-z^2/2L_h^2)\sin(k_0 z). \tag{6}$$

The same function can be written in the spectral domain as

$$H(k,k_0,L_h) = \frac{j}{2}(\exp(-(k+k_0)^2 L_h^2/2)$$

$$-\exp(-(k-k_0)^2 L_h^2/2)), \tag{7}$$

where we have used the Fourier transform convention

$$h(z) = \frac{1}{2\pi} \int dk\, H(k)\exp(-jkz),$$

$$\tag{8}$$

$$H(k) = \int dz\, h(z)\exp(jkz).$$

Prior to compression, the system response is $H_1(k) = H(k,k_0,L_h)$. After compression, we may wish to modify the system response function by changing the wavelength of the sinusoid and the correlation length. These new parameters are denoted by primed quantities in the system response for the postcompression waveform, $H_2(k) = H(k,k_0',L_h')$.

The reflectivity profile $f(z)$ is modeled by filtering a white noise process by the function $p(z)$. In tissue, the longitudinal microstructural variation is often represented by a Gaussian autocorrelation function.[28,29] A filter function that approximates such structural variations is also a Gaussian function[30] that is centered at spatial frequency k_f,

$$P(k) = \tfrac{1}{2}(\exp(-(k+k_f)^2 L_f^2/2) + \exp(-(k-k_f)^2 L_f^2/2)), \tag{9}$$

where L_f is a correlation length of the reflectivity profile. In Sec. II, we use the reflectivity spectral autocorrelation function, $\langle F^*(k_1)F(k_2)\rangle$, where $\langle.\rangle$ denotes the ensemble aver-

age operator and * is the complex conjugate operator. One can show that

$$\langle F^*(k_1)F(k_2)\rangle = N_0 P^*(k_1)P(k_2)\delta(k_1-k_2), \qquad (10)$$

where N_0 is the power spectrum level of the uncorrelated noise process from which the reflectivity profile is realized. The reflectivity profile function is real, therefore the conjugate symmetric property, $F^*(k)=F(-k)$, is satisfied.

C. Modeling the strain profile

Little is known about the strain patterns that are produced in biological tissues under uniform loading conditions. We suggest that the axial strain profile can be described as the sum of a mean value $\bar{s}$ and perturbation about the mean δs, i.e.,

$$s(z)=\bar{s}+\delta s(z). \qquad (11)$$

Consider two types of strain profile, namely, deterministic and stochastic. A deterministic strain profile is known exactly, so that the mean value is given by

$$\bar{s}=\frac{1}{L}\int_0^L s(\gamma)d\gamma = \frac{L-L'}{L}, \qquad (12)$$

where L and L' are the axial lengths of the tissue before and after the compression, respectively. With this notation, $s(z)\geq 0$.

A stochastic strain profile is a random variable for which there is complete prior knowledge of its statistical properties. We define the mean as the ensemble average

$$\bar{s}=\langle s(z)\rangle, \qquad (13)$$

and assume that the strain perturbation δs is a wide-sense stationary, Gaussian-distributed random process with mean zero and variance σ_s^2. The second-order statistics of δs may be described by an exponential autocorrelation function

$$\langle \delta s(z)\delta s(z')\rangle = \sigma_s^2 \exp(-|z-z'|/L_s), \qquad (14)$$

a Gaussian autocorrelation function

$$\langle \delta s(z)\delta s(z')\rangle = \sigma_s^2 \exp(-(z-z')^2/L_s^2) \qquad (15)$$

or a second derivative of a Gaussian (2DG)

$$\langle \delta s(z)\delta s(z')\rangle = \sigma_s^2(1-2(z-z')^2/L_s^2)$$
$$\times \exp(-(z-z')^2/L_s^2), \qquad (16)$$

where L_s denotes the correlation length of the stochastic strain profile. We assume that the strain profile varies more slowly than the reflectivity profile, so that $L_f < L_s$.

For the deterministic and stochastic cases, the effect of strain is to deform the longitudinal coordinate axis of the reflectivity profile, z. This produces a postcompression reflectivity profile with a different depth dependence than the precompression reflectivity profile. The relation between the two is

$$f_2(z'=g(z))=f_1(z), \qquad (17)$$

where the transformation for axial strain is defined by

$$z'=g(z)=\int_0^z (1-s(\gamma))d\gamma. \qquad (18)$$

If the strain is two or three dimensional and the lateral and/or elevational displacement is greater than the beamwidth, then some scatterers leave the beam as new scatterers enter. In that case, we cannot express f_2 as a rescaled copy of f_1 as in Eq. (17).

To write the postcompression reflectivity profile f_2 as a function of the precompression coordinate z, we need the inverse relation $g^{-1}(z')$. However an inverse relation is not easily expressible for an arbitrary strain profile. In the Appendix, we show that the inverse transform can be approximated from Eq. (18) for small strains by

$$z\approx \int_0^{z'/(1-\bar{s})}\left(1+\frac{\delta s(\gamma)}{1-\bar{s}}\right)d\gamma. \qquad (19)$$

With the above coordinate transformation, the postcompression reflectivity profile can be written in terms of the precompression coordinate axis,

$$f_2(z)\approx f_1\left[\frac{z}{1-\bar{s}}+\beta\left(\frac{z}{1-\bar{s}}\right)\right], \qquad (20)$$

where $\beta(z)$ denotes the displacement given by the integral of the strain perturbation

$$\beta(z)=\frac{1}{1-\bar{s}}\int_0^z \delta s(\gamma)d\gamma. \qquad (21)$$

It has been suggested that there are advantages to stretching r_2 by the average or local strain $\bar{s}$ in a preprocessing step before cross correlation with r_1.[4] In that case, the stretched echo signal, denoted by the subscript 3, becomes

$$r_3(z)=r_2((1-\bar{s})z)$$
$$\text{for the stretched postcompression signal.} \qquad (22)$$

The advantages of stretching the postcompression signal are discussed later in Sec. III. Combining Eqs. (5) and (22), we find that $f_3(z)=f_2((1-\bar{s})z)$, and from Eq. (20)

$$f_3(z)\approx f_1(z+\beta(z)). \qquad (23)$$

Since $\langle\beta(z)\rangle=0$, then $\langle\beta^2(z)\rangle$ is the variance of the displacement in the stochastic problem. We note the similarity of Eq. (21) and the right side of Eq. (23) with the equations that describe frequency modulation in communication theory.[31] When the reflectivity profile is sinusoidal, then loading the tissue and stretching the resulting reflectivity profile by the average displacement generates the same equations as those found in the problem of extracting information from frequency-modulated signals.

II. ANALYTICAL RESULTS

In this section, we derive the cross-correlation function between pre- and postcompression signals. Under the assumption of zero-mean noise that is signal independent and spatially uncorrelated, we concentrate entirely on evaluating the two-point ensemble average taken at depths z_1 and z_2:

$$\Gamma_{12}(z_1,z_2)=\langle r_1(z_1)r_2(z_2)\rangle$$
$$=\langle(h_1(z_1)\otimes f_1(z_1))(h_2(z_2)\otimes f_2(z_2))\rangle. \quad (24)$$

We will provide analytic formulas of the above cross correlation for the deterministic and random strain profiles, and show that the cross correlation is not stationary in the statistical sense. The resulting equations are used to interpret the effects of static compression on the signal decorrelation and the variance of the tissue displacement.

A. Deterministic problem

A schematic of the 1-D deterministic problem is shown in Fig. 2. The figure exhibits an enlarged version of the thin vertical bar shown at the center of the tissue in Fig. 1. The bar is segmented into three layers of different elasticities and therefore strains. Regions I and III are soft background and region II is a hard inclusion. The inclusion is of size $2R$ and is centered at depth Z in a sample of precompression axial length L. Under static compression, region II strains by an amount s_2. Similarly, background regions I and III strain by amounts s_1 and s_3, respectively. The average strain as calculated from Eq. (12) is

$$\bar{s}=\{s_3 L+(s_1-s_3)Z+(2s_2-s_1-s_3)R\}/L. \quad (25)$$

The average strain is measured in an experiment from the displacement of the compressor-transducer assembly after compression. The reflectivity profile of the compressed tissue f_2 is related to the pre-compression reflectivity profile f_1 by following the transformation rule of Eq. (18):

$$f_2(z)=f_1(az-b), \quad (26)$$

where the variables a and b take the following forms for the three regions:

$$\begin{cases} a=1/(1-s_1), & b=0 \quad \text{for } 0\leq z<Z_1, \\ a=1/(1-s_2), & b=(s_2-s_1)(Z-R)/(1-s_2) \quad \text{for } Z_1\leq z<Z_2, \\ a=1/(1-s_3), & b=(s_3-s_1)Z+(s_1+s_3-2s_2)R/(1-s_3) \quad \text{for } Z_2\leq z<(1-\bar{s})L, \end{cases} \quad (27)$$

and

$$Z_1=(1-s_1)(Z-R),$$
$$Z_2=(1-s_1)(Z-R)+2(1-s_2)R. \quad (28)$$

If the strain is uniform ($s_1=s_2=s_3$), then $b=0$ for all z.

The cross-correlation function between echo signals r_1 and r_2 is found by considering any two points z_1 and z_2 located in one of the three regions. Equation (24) can be written in the Fourier domain as

$$\Gamma_{12}(z_1,z_2)=\frac{1}{(2\pi)^2 a}\int\int dk_1\,dk_2\,H_1^*(k_1)H_2(k_2)$$
$$\times\left\langle F_1^*(k_1)F_1\left(\frac{k_2}{a}\right)\right\rangle$$
$$\times\exp\left[j\left(k_1 z_1-k_2 z_2+\frac{k_2 b}{a}\right)\right], \quad (29)$$

where the values of a and b depend on the region as defined by Eq. (27). We used the conjugate symmetric property of the reflectivity function $f_1(z)$. After substituting Eq. (10) into Eq. (29) and evaluating the integral over k_2, we obtain

$$\Gamma_{12}(z_1,z_2)$$
$$=\frac{N_0}{2\pi}\int dk_1\,H^*(k_1,k_0,L_h)H(ak_1,k_0',L_h')$$
$$\times|P(k_1)|^2\exp(j(az_2-z_1+b)k). \quad (30)$$

Carrying out the above calculation with the system response and the filter functions defined in Eqs. (7) and (9), respectively, we find that

$$\Gamma_{12}(z_1,z_2)=\frac{N_0}{16\sqrt{\pi}\,\eta_a}\exp\left[-\tau_a^2+\left(\frac{\zeta_a^2}{\eta_a^2}\right)\right]$$
$$\times\exp\left(-\frac{(z_1-az_2+b)^2}{4\eta_a^2}\right)$$
$$\times\cos\left(\frac{\zeta_a(z_1-az_2+b)}{\eta_a^2}\right), \quad (31)$$

where

$$\eta_a^2=L_f^2+\frac{L_h^2+a^2 L_h'^2}{2},$$
$$\tau_a^2=k_f^2 L_f^2+\frac{k_0^2 L_h^2+k_0'^2 L_h'^2}{2}, \quad (32)$$
$$\zeta_a=k_f L_f^2+\frac{k_0 L_h^2+a k_0' L_h'^2}{2}.$$

The estimation problem in elastography is to determine the displacement z_1-z_2 that best aligns the two echo waveforms. That occurs at the correlation lag corresponding to the peak value of Γ_{12}. Equation (30) is similar to the normalized cross-correlation function of Walker and Trahey [Ref. 32, Eq. (19)]. Their expression is for a constant strain profile, bandpass white pulse spectrum, and white-noise scattering function, e.g., uncorrelated point scatterers. Above are more general expressions for a variable strain profile that is known, Gaussian pulse spectrum, and scattering medium with finite-size scatterers.

B. Stochastic problem

For the deterministic problem in the previous subsection, we were able to compute $f_2(z)$ exactly, as in Eqs. (26)–(28). For the stochastic problem, however, $f_2(z)$ cannot be found in the same manner. Instead, we use the approximation, Eq. (19), for the coordinate transformation, Eq. (18). From Eqs. (10) and (20), we find that Eq. (24) yields

$$\Gamma_{12}(z_1,z_2) = \frac{N_0}{(2\pi)^2} \int \int dk_1 \, dk_2 \, H_1^*(k_1) H_2(\bar{a} k_2) |P(k_1)|^2$$

$$\times \exp(j(k_1 z_1 - \bar{a} k_2 z_2)) \int dz'$$

$$\times \exp(j(k_2 - k_1)z') \langle \exp(-jk_1\beta(z')) \rangle, \quad (33)$$

where $\bar{a} = 1/(1-\bar{s})$.

The function $\beta(.)$ is defined in Eq. (21) as the cumulative strain perturbation. Since δs is defined as a zero-mean Gaussian random process, its integral is also a Gaussian process. The characteristic function of the Gaussian random variable q is $\langle \exp(iq) \rangle = \exp(-\langle q^2 \rangle/2)$,[31] so that

$$\langle \exp(-jk_1\beta(z')) \rangle = \exp\left(-\frac{k_1^2}{2} \langle \beta^2(z') \rangle \right). \quad (34)$$

The variance $\langle \beta^2(z') \rangle$ in the above equation is calculated using Eq. (21) as

$$\langle \beta^2(z') \rangle = \bar{a}^2 \int_0^{z'} \int_0^{z'} d\gamma \, d\mu \langle \delta s(\gamma) \delta s(\mu) \rangle, \quad (35)$$

where the expectation, $\langle \delta s(\gamma) \delta s(\mu) \rangle$, is defined by Eqs. (14)–(16) for the three autocorrelation models under consideration.

Substituting Eq. (14) into Eq. (35) and evaluating the integrals for the exponential autocorrelation function, we obtain

$$\langle \beta_E^2(z') \rangle = \bar{a}^2 \sigma_s^2 L_s^2 \left[\exp\left(-\frac{|z'|}{L_s} \right) + \frac{|z'|}{L_s} - 1 \right]. \quad (36)$$

Similarly, Eqs. (15) and (16) yield

$$\langle \beta_G^2(z') \rangle = \bar{a}^2 \sigma_s^2 L_s^2 \left\{ \exp(-z'^2/L_s^2) - 1 \right.$$

$$\left. + \sqrt{\pi} \frac{z}{L_s} \, \mathrm{erf}(z'/L_s) \right\} \quad (37)$$

and

$$\langle \beta_{2DG}^2(z') \rangle = \bar{a}^2 \sigma_s^2 L_s^2 \{ 1 - \exp(-z'^2/L_s^2) \} \quad (38)$$

for the Gaussian and second derivative of the Gaussian (2DG) autocorrelation functions. These equations are the displacement variances for the three autocorrelation models.

Next, we investigate the integral

$$\int dz' \, \exp(j(k_2-k_1)z') \exp\left(-\frac{k_1^2}{2} \langle \beta^2(z') \rangle \right) \quad (39)$$

in Eq. (33) for the special cases of Eqs. (36)–(38). Substituting Eq. (36) into Eq. (39), we find a series solution using an identity given by Middleton.[33] Substituting that series solution back into Eq. (33), however, we were unable to find closed form solutions for the assumed system response $H(.)$

and the filter $P(.)$ functions. Furthermore, we could not evaluate the integral in Eq. (39) for the Gaussian form, Eq. (37). A series solution for Eq. (39) was obtained with the 2DG form of Eq. (38). However, the resulting expression provides no intuition regarding the basic physics of the problem. Since closed form solutions of Eq. (33) were not found for the assumed autocorrelation models, we decided to evaluate the lower bounds of Γ_{12}, since any improvement in the lower bound implies an increase in the magnitude of the cross correlation.

By analyzing the large z' dependence of Eqs. (36)–(38), one can show that the variances are bounded according to

$$\langle \beta^2(z') \rangle \leq C, \quad (40)$$

where

$$C = \begin{cases} \bar{a}^2 \sigma_s^2 L_s L & \text{for the exponential autocorrelation} \\ & \text{function,} \\ \sqrt{\pi} \bar{a}^2 \sigma_s^2 L_s L & \text{for the Gaussian autocorrelation} \\ & \text{function,} \\ \bar{a}^2 \sigma_s^2 L_s^2 & \text{for the 2DG autocorrelation function.} \end{cases} \quad (41)$$

Note that the values of C for different autocorrelation models are very similar. The smallest C value is for the 2DG model, since the correlation length of the strain profile L_s is much smaller than the length of the sample L. From the variance bound, it is clear that the integral in Eq. (39) has a lower bound given by

$$\int dz' \, \exp(j(k_2-k_1)z') \exp\left(-\frac{k_1^2}{2} \langle \beta^2(z') \rangle \right)$$

$$\geq \exp\left(-\frac{C}{2} k_1^2 \right) \delta(k_2-k_1). \quad (42)$$

Substituting this expression into Eq. (33) and evaluating the integrals we obtain the worst case scenario for the cross correlation:

$$\Gamma_{12}(z_1,z_2) \geq \frac{N_0}{16\sqrt{\pi}\,\eta_{\bar{a}}'} \exp\left[-\tau_{\bar{a}}^2 + \left(\frac{\zeta_{\bar{a}}^2}{\eta_{\bar{a}}'^2} \right) \right]$$

$$\times \exp\left(-\frac{(z_1-\bar{a}z_2)^2}{4\eta_{\bar{a}}'^2} \right) \cos\left(\frac{\zeta_{\bar{a}}(z_1-\bar{a}z_2)}{\eta_{\bar{a}}'^2} \right), \quad (43)$$

where

$$\eta_{\bar{a}}'^2 = L_f^2 + \frac{L_h^2 + \bar{a}^2 L_h'^2}{2} + \frac{C}{2} \quad (44)$$

and $\tau_{\bar{a}}^2$ and $\zeta_{\bar{a}}$ are obtained from Eq. (32) by substituting $\bar{a}$ in place of a. There is a strong similarity between the results of the deterministic and stochastic problems, Eqs. (31) and (43).

$\Gamma(z_1, z_2) \qquad \eta'/\zeta$
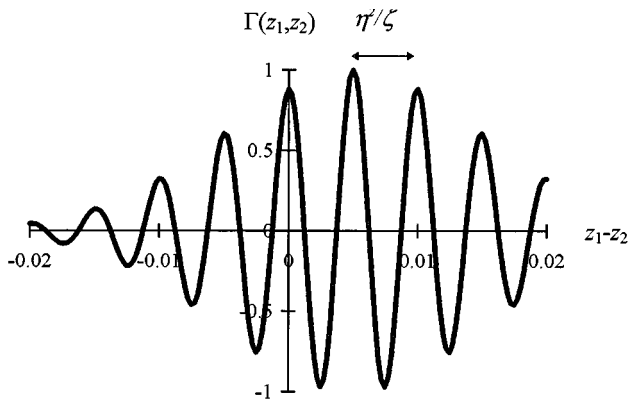
FIG. 3. Shows a typical cross-correlation function. The period of the oscillation is η'^2/ζ.

In the next section, we show how Γ_{12} for the deterministic and stochastic cases depend on parameters of the imaging system and the medium under investigation. Then, we isolate the variables critical to maximizing the cross-correlation function.

III. DISCUSSION AND EXAMPLES

A. Deterministic problem

Consider the results of Sec. II A, where the strain profile has three well-defined layers. The cross-correlation function for this deterministic problem is described by Eq. (31) and is plotted in Fig. 3 for typical broadband echo signals. The first exponential factor on the right-hand side of Eq. (31) scales $\Gamma_{12}(z_1, z_2)$ independent of position in the medium. The second exponential factor gives the envelope of $\Gamma_{12}(z_1, z_2)$ its Gaussian shape. The cosine factor determines the oscillation frequency and phase of $\Gamma_{12}(z_1, z_2)$. Our objective is to design experiments so that the peak value of $\Gamma_{12}(z_1, z_2)$ is maximized with respect to the noise and is large compared to adjacent peaks. Any process that reduces the maximum cross-correlation value is a source of signal decorrelation that should be minimized.

For low input signal-to-noise conditions (S/N is the ratio of echo-signal power to noise power), the second exponential factor and the cosine factor dominate the strain variance because of ambiguity error.[34,35] To reduce this error and correctly distinguish among the cross-correlation peaks, we could design the experiment to minimize η_a^2 so that the envelope of $\Gamma_{12}(z_1, z_2)$ attenuates the adjacent peaks. Alternatively, we could minimize ζ_a/η_a^2, which increases the separation between cross-correlation peaks. In either case, ambiguity error is minimized for low input S/N when we use low center frequency and/or broadband pulses.

For the high input S/N conditions common in medical imaging, the first exponential factor in Eq. (31), $\exp(-\tau_a^2 + \zeta_a^2/\eta_a^2)$, is the major factor determining estimation variance. Displacement uncertainty is due primarily to decorrelation between the pre- and postcompression echo signals. Decorrelation may be viewed as a mismatch between the pre- and postcompression echo spectra. Spectral changes caused by tissue motion have been discussed in detail by

Kallel *et al.*[15] Signal decorrelation is minimum when $-\tau_a^2 + \zeta_a^2/\eta_a^2 = 0$, which may be achieved using one of three strategies.

The first strategy is to increase the bandwidth of the pulse so it is large compared with the bandwidth of the tissue spectrum, i.e., $L_h \cong L_h' \ll L_f$. Each scatterer is then resolved and can be tracked individually. Unfortunately, very broadband transducers with sufficient sensitivity to penetrate deep into the body are not currently available.

The second strategy is to keep the strains small, $a \cong 1$, and to match the pulse and tissue spectra, $H_1(k) \cong F_1(k)$. However, small strains produce weak elastographic signals, which result in low target visibility. Also, if hard inclusion with different elastic moduli are placed in a soft background, then large compressions are required to obtain the dynamic range necessary to differentiate among the hard inclusions.

The third strategy is most promising for many practical situations that call for moderate pulse bandwidths and moderate tissue strains. As with the second strategy, we choose a pulse spectrum that matches the tissue spectra, but in addition we apply two conditioning steps to the postcompression echo signal, viz., pulse shaping and signal stretching, so that $H_1(k) \cong F_1(k) \cong H_2(k) \cong F_2(k)$ even for moderately large strains.

1. Shaping the postcompression pulse, $h_2(z)$

To illustrate the value of signal conditioning, we define two parameters that quantify the amount of echo-signal decorrelation. The correlation coefficient ρ measures the similarity of two signals, and is defined as

$$\rho \equiv \frac{\Gamma_{12\,\text{max}}}{\sqrt{\Gamma_{11\,\text{max}}\Gamma_{22\,\text{max}}}}. \tag{45}$$

The peak-ratio PR is another measure of similarity that also compares signal amplitudes:

$$\text{PR} \equiv \frac{\Gamma_{12\,\text{max}}}{\Gamma_{11\,\text{max}}}. \tag{46}$$

$\Gamma_{11\,\text{max}}$ and $\Gamma_{22\,\text{max}}$ are peak autocorrelation function values for the echo signals r_1 and r_2.

To study the cross-correlation peak for constant-strain conditions, we isolate the first exponential factor in Eq. (31) by setting $z_1 - az_2 + b = 0$ and then evaluating PR of Eq. (31) to find

$$\text{PR} = \sqrt{\frac{L_f^2 + L_h^2}{\eta_a^2}} \exp\left(\frac{k_0^2 L_h^2 - k_0'^2 L_h'^2}{2} + \frac{\zeta_a^2}{\eta_a^2} \right.$$
$$\left. - \frac{(k_f L_f^2 + k_0 L_h^2)^2}{L_f^2 + L_h^2} \right). \tag{47}$$

Substituting $aL_h' = L_h$ and $k_0' = ak_0$ into Eq. (47), we find that PR = 1; that is, the pre- and postcompression signals are perfectly aligned and there is no signal decorrelation. The correlation coefficient ρ is also unity under the above conditions. With that substitution, we increase the center frequency k_0' and reduce the length L_h' of the postcompression ultrasound pulse by the scale factor $a = 1/(1-s)$. This preserves the product $L_h' k_0' = L_h k_0$. Since ρ and PR are both

3218   J. Acoust. Soc. Am., Vol. 99, No. 5, May 1996

M. Bilgen and M. F. Insana: Deformation models in elasticity   3218
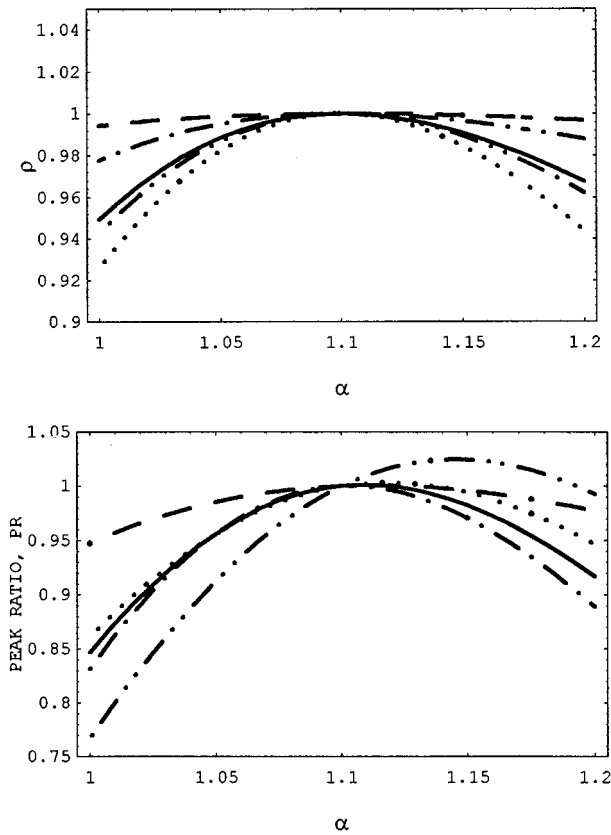
FIG. 4. Shows the dependence of the correlation coefficient ρ (top) and the peak ratio PR (bottom) on the scaling parameter α for the deterministic problem when $a=1.1$ and $k_0=2\pi/0.3$ mm^{-1}. Solid line: $k_f=k_0$, $L_f=L_h=0.3$ mm, dotted line: $k_f=k_0$, $L_f=0.15$ mm, $L_h=0.3$ mm, dashed line: $L_f=0.3$ mm, $L_h=0.15$ mm, dot-dashed line: $k_f=k_0$, $L_f=0.6$ mm, $L_h=0.3$ mm, and dot-dot-dashed line: $k_f=1.05k_0$, $L_f=0.3/1.05$ mm, $L_h=0.3$ mm.

one, it may be possible to eliminate signal decorrelation for moderate strains provided that parameters of the impulse response function $h_2(z)$ are compressed at the same rate as the medium.

In most experimental situations, the strain profile, and therefore the parameter a, is unknown and varies with depth, i.e., $a(z)$. It is worthwhile, then, to study how ρ and PR change when scaling the postcompression point spread function according to a constant scale factor α.[36] That is, for $H_2(k) = H(k,k_0',L_h')$, let $L_h' = L_h/\alpha$, $k_0' = \alpha k_0$ and $\alpha \geq 1$. With this scaling, we find

$$\rho = \frac{(L_f^2+L_h^2)^{1/4}((a/\alpha)^2 L_f^2+L_h^2)^{1/4}}{\eta_{a/\alpha}} \exp\left(\frac{\zeta_{a/\alpha}^2}{\eta_{a/\alpha}^2}\right.$$
$$\left. -\frac{1}{2}\left\{\frac{(k_f L_f^2+k_0 L_h^2)^2}{L_f^2+L_h^2}+\frac{(k_f L_f^2+(a/\alpha)k_0 L_h^2)^2}{(a/\alpha)^2 L_f^2+L_h^2}\right\}\right)$$
(48)

and

$$\mathrm{PR}=\sqrt{\frac{L_f^2+L_h^2}{\eta_{a/\alpha}^2}} \exp\left(\frac{\zeta_{a/\alpha}^2}{\eta_{a/\alpha}^2}-\frac{(k_f L_f^2+k_0 L_h^2)^2}{L_f^2+L_h^2}\right). \qquad (49)$$

Equations (48) and (49) are plotted in Fig. 4 as a function of α for a constant strain of 10% ($a=1/(1-0.1)\approx 1.1$). The in-

terrogating pulse is assumed to have a wavelength and correlation length of 0.3 mm. The solid lines in the figures represent the perfect alignment case where the pulse and tissue spectra are exactly matched, i.e., $k_f=k_0$ and $L_f=L_h=0.3$ mm. There is no decorrelation at $\alpha=a$, where we scale the pulse in the same manner as the tissue compression scales the axial coordinate of reflectivity spectrum. The dotted curves are for $k_f=k_0$ and $L_f=0.15$ mm, $L_h=0.3$ mm, the dashed curves are for $k_f=k_0$ and $L_f=0.3$ mm, $L_h=0.15$ mm, the dot-dashed curves are for $k_f=k_0$ and $L_f=0.6$ mm, $L_h=0.3$ mm, and the dot-dot-dashed curves are for $k_f=1.05k_0$ and $L_f=0.3/1.05$ mm, $L_h=0.3$ mm. The broken lines represent conditions where the pulse and tissue spectra are not exactly matched.

Figure 4 shows that $\rho=0.95$ and PR$=0.85$ when there is no pulse shaping ($\alpha=1.0$). Both functions rise to unity at $\alpha=1.1$, and fall to $\rho=0.97$ and PR$=0.92$ at $\alpha=1.2$. Less decorrelation occurs when the pulse spectrum is broader than the tissue spectrum (dashed curves).

The situation is different for the other cases considered. Varying the width of the tissue spectrum for a constant pulse spectrum (dotted curves and dot-dashed curves) has severe effects on ρ but little effect on PR. The values of ρ for $\alpha=1$ are 0.92 and 0.98, indicating that the effect on ρ is more pronounced for $L_f<L_h$ (dotted curves) and less pronounced for $L_f>L_h$ (dot-dashed curves). Varying the tissue spectra lowers PR to 0.85 when $\alpha=1$.

The reflectivity spectra for most tissues are unknown, so it is likely that the spectra for the pulse and the tissue will not be matched. For example, the dot-dot-dashed lines in Fig. 4 represents the results for $k_f/k_0=1.05$. Because the center frequencies are not matched, the peak in the PR versus α curve, Eq. (49), is greater than one. In fact, anytime $k_f\neq k_0$, the peak of the PR versus α curve will be greater than one: the peak is located at $\alpha>a$ for $k_f>k_0$ and at $\alpha<a$ for $k_f<k_0$. The advantage of PR over ρ is its ability to detect conditions where $k_f\neq k_0$. We can exploit the additional information provided by PR using an iterative strategy: k_0 is adjusted until the peak of the PR versus α curve is approximately one. At that point, the center frequencies of the pulse and tissue spectra are matched.

The *estimated* tissue spectrum may not well approximate the *expected* tissue spectrum, $F(k)$, under any measurement conditions that demand spatial resolution. Short-duration waveform segments yield noisy estimates of $F(k)$. Consequently, even when $k_f=k_0$, the PR versus α curve may not peak at one. As the amount of stationary independent data increases, we approach the results of Fig. 4. However, time averaging is not equivalent to ensemble averaging for estimating the cross-correlation function. At the peak value of $\Gamma_{12}(z_1,z_2)$ in Eq. (31), $z_1-az_2+b=0$, so that $\Delta z\equiv z_1-z_2=(1-a)z_2+b$. In words, the cross-correlation lag corresponding to the displacement estimate Δz is a function of axial position z_2, so that the postcompression echo signal r_2 is a nonstationary random process. The greater the strain, the more nonstationary the signals become.

3219   J. Acoust. Soc. Am., Vol. 99, No. 5, May 1996

M. Bilgen and M. F. Insana: Deformation models in elasticity   3219

(a)

$H_2 = H_1$

$F_1 \rightarrow F_2$

a/L_f

$k_0 \quad k_f \quad ak_f \quad k$

(b)

$H_1 \rightarrow H_2$

$F_1 \rightarrow F_2$

$k_0 \ ak_0 \qquad k_f \ ak_f \qquad k$

(c)

$H_1 \leftarrow H_2$

$F_1 \leftarrow F_2$

$k_0 \qquad k_f \qquad k$
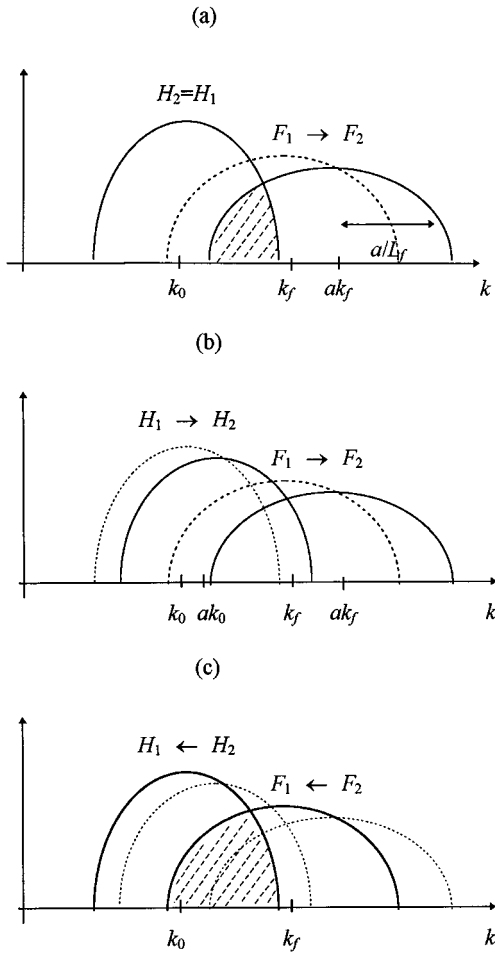
FIG. 5. Spectral effects of conditioning the postcompression echo signal are illustrated. (a) Without signal conditioning, the height of the cross-correlation function $\Gamma(z_1, z_2)$ at its peak, $z_2 = (z_1 + b)/a$, is given by the cross-hatched area via Eqs. (29)–(31). The center frequency and bandwidth of the postcompression reflectivity spectrum F_2 are shifted by the factor $a = 1/(1-s)$ because of compression. (b) The compressed tissue may be interrogated by pulse spectrum H_2 that has been modified in the same manner as the tissue spectrum. (c) Stretching the echo signal by the factor $1/a$ provides a good match between the pre- and postcompression spectra. As a result, the height of the cross-correlation peak (cross-hatched area) is greater for the conditioned signals in part (c) than for the unconditioned signals in part (a).

2. Stretching the postcompression echo signal, r_2

We can reduce the dependence of the cross-correlation function on position z_2 by scaling the axial coordinate according to the relation $r_3(z_3) = r_2((1-\bar{s})z_3)$ before performing the cross correlation. Scaling the coordinate z_2 is equivalent to stretching the postcompression echo signal $r_2(z_2)$. Following the development in Sec. III A, it is straightforward to derive $\Gamma_{13}(z_1, z_3)$. The only difference is the arguments of the last two factors on the right-hand side of Eq. (31) change from $(z_1 - az_2 + b)$ to $(z_1 - (1-\bar{s})az_3 + b)$. The correlation lag at the peak of $\Gamma_{13}(z_1, z_3)$ is $\Delta z = z_1 - z_3 = (1 - (1-\bar{s})a)z_3 + b$. For a homogeneous strain profile, where $a = 1/(1-\bar{s})$, r_3 is a stationary process. The effects of pulse shaping and stretching are illustrated in Fig. 5. For inhomogeneous strain profiles, the positional dependence of the correlation lag is not eliminated but weakened, since $|(1-\bar{s})a| \leqslant |a|$. In elastography, we assume the echo signals are
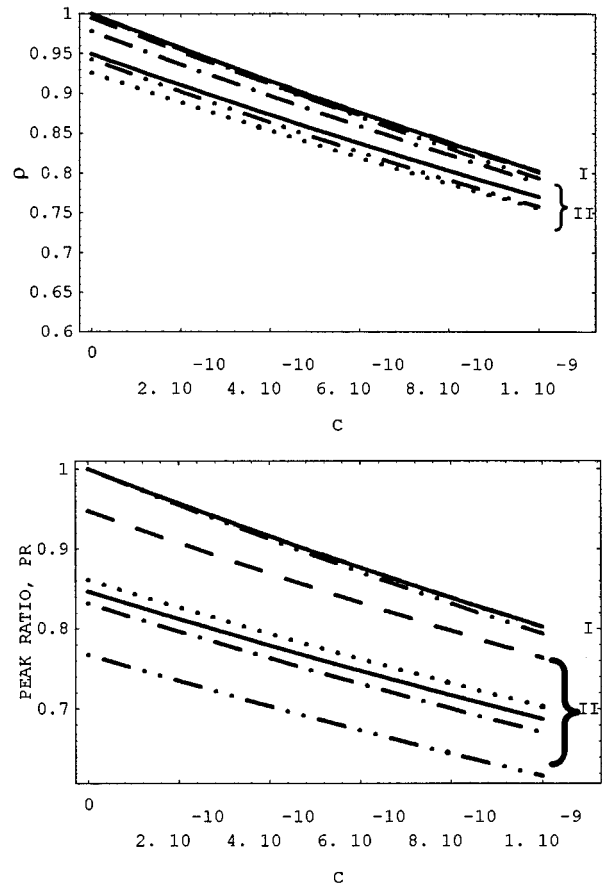

FIG. 6. Shows the dependence of the correlation coefficient ρ (top) and the peak ratio PR (bottom) on constant C for the stochastic problem. The identification (I) is for $\alpha = \bar{a} = 1.1$ and (II) is for $\alpha = 1.0$ and $\bar{a} = 1.1$. $k_0 = 2\pi/0.3$ mm^{-1}, solid lines: $k_f = k_0$, $L_f = L_h = 0.3$ mm, dotted lines: $k_f = k_0$, $L_f = 0.15$ mm, dashed lines: $L_f = 0.3$ mm, $L_h = 0.15$ mm, dot-dashed lines: $k_f = k_0$, $L_f = 0.6$ mm, $L_h = 0.3$ mm, and dot-dot-dashed lines: $k_f = 1.05k_0$, $L_f = 0.3/1.05$ mm, $L_h = 0.3$ mm.

wide-sense stationary over the window length W, so that the spatial average $W \int_{-W/2}^{W/2} r_1(z_2 - z) r_2(z_2) dz_2$ may be used to estimate the ensemble average $\langle r_1(z_1) r_2(z_2) \rangle$. Stationarity is more nearly achieved when the postcompression signal is linearly stretched according to the mean strain, particularly when the strain variations along the profile are small, e.g., for inclusions with low elastic contrast.

B. Stochastic problem

Consider the results of Sec. II B, where the strain profile for the entire sample length is known statistically. The cross-correlation function for this stochastic problem, Eq. (43), is very similar to that of the deterministic problem, Eq. (31). In the limit where the variations in strain are zero, the bound value C in Eq. (41) is zero and the two equations are equal. If the statistical properties of the strain variations δs are known, then Eq. (43) may be used to design measurements that minimize the uncertainty in displacement estimates in a manner similar to the discussion above for the deterministic problem.

The values of C corresponding to the Gaussian and exponential models for strain correlation, Eq. (41), are very conservative in the sense that they probably overestimate the amount of decorrelation error caused by actual strain varia-

tions. The second derivative of the Gaussian (2DG) may be a more realistic model for describing the second-order statistics of strain variations in tissue. The zero-mean feature of the function is consistent with the notion that strain is conserved. Unlike the Gaussian and exponential forms, the 2DG model does not accumulate errors caused by strain variations throughout the entire sample length L. It emphasizes local variations, which results in reduced values for C and less signal decorrelation.

We now examine ρ and PR obtained from Eqs. (41)–(44),

$$\rho \geqslant \frac{(L_f^2+L_h^2)^{1/4}((\bar{a}/\alpha)^2 L_f^2+L_h^2)^{1/4}}{\eta'_{\bar{a}/\alpha}} \exp\left(\frac{\zeta_{\bar{a}/\alpha}^2}{\eta'^2_{\bar{a}/\alpha}} \right.$$
$$\left. -\frac{1}{2}\left\{ \frac{(k_f L_f^2+k_0 L_h^2)^2}{L_f^2+L_h^2} + \frac{(k_f L_f^2+(\bar{a}/\alpha)k_0 L_h^2)^2}{(\bar{a}/\alpha)^2 L_f^2+L_h^2}\right\} \right)$$

(50)

and

$$\mathrm{PR} \geqslant \sqrt{\frac{L_f^2+L_h^2}{\eta'^2_{\bar{a}/\alpha}}} \exp\left(\frac{\zeta_{\bar{a}/\alpha}^2}{\eta'^2_{\bar{a}/\alpha}} - \frac{(k_f L_f^2+k_0 L_h^2)^2}{L_f^2+L_h^2} \right).$$

(51)

We are particularly interested in the dependence of ρ and PR on the constant C whose values are given in Eq. (41) for all three autocorrelation models. Figure 6 illustrates how strain variance increases signal decorrelation through ρ and PR. Curves labeled I and II in Fig. 6 are for $\alpha = \bar{a} = 1.1$ and $\alpha = 1.0$, respectively; at $C = 0$ the values in Fig. 6 are the same as those in Fig. 4. Solid curves are calculated for $k_f = k_0$ and $L_f = L_h = 0.3$ mm; the dotted curves are for $k_f = k_0$ and $L_f = 0.15$ mm, $L_h = 0.3$ mm; the dashed curves are for $k_f = k_0 L_h = 0.15$ mm; the dot-dashed curves are for $k_f = k_0$ and $L_f = 0.6$ mm, $L_h = 0.3$ mm; and the dot-dot-dashed curves are for $k_f = 1.05 k_0$ and $L_f = 0.3/1.05$ mm, $L_h = 0.3$ mm. Figure 6 shows that echo-signal correlation is reduced as C increases. The decline in ρ at greater strain

variability is slower than it is for PR. The decline for PR is almost at the same rate for all the above configurations studied. The rate of decorrelation is approximately equal to

$$\frac{(k_f L_f^2+k_0 L_h^2)^2}{2(L_f^2+L_h^2)^2}.$$

(52)

Equation (41) gives the values of C for the three autocorrelation models that describe the random strain field. The 2DG strain model predicts that strain variability causes much less signal decorrelation than the Gaussian model. Experimental studies are needed to determine which if any of these models for δs is most appropriate.

Further examination of Eqs. (43) and (44) shows that the main effect of strain variations on Γ_{12} for high input S/N is to reduce its amplitude via the first exponential factor on the right-hand side. The reduction in peak amplitude is caused by echo-signal decorrelation. At low input S/N, the strain variance improves displacement estimation performance by increasing the period of Γ_{12} oscillations via the cosine factor, but also hinders performance by increasing the width of the Gaussian roll-off via the second exponential factor. Overall, random strain variations are expected to increase displacement uncertainty by an amount that depends on statistical properties of the strain variation. As with the deterministic problem, pulse scaling and linear stretching minimize echo-signal decorrelation caused by inhomogeneities in the strain profile.

C. Testing the validity of Eq. (19)

The reliability of the results for the stochastic problem in the previous section depends on the accuracy of the approximate inverse-coordinate transformation given by Eq. (19). We used the three-layer deterministic example diagrammed in Fig. 2 to assess the accuracy of the approximation. Equation (20) provides estimates of the reflectivity profiles in the three regions:

$$f_{2\,\mathrm{app}}(z)=\begin{cases} f_1((1+\bar{a}(s_1-\bar{s}))\bar{a}z), & 0\leqslant z<Z_1, \\ f_1((1+\bar{a}(s_2-\bar{s}))\bar{a}z+\bar{a}^2(s_1-s_2)Z_1), & Z_1\leqslant z<Z_2, \\ f_1((1+\bar{a}(s_3-\bar{s}))\bar{a}z+\bar{a}^2(s_1-s_2)Z_1+\bar{a}^2(s_2-s_3)Z_2), & Z_2\leqslant z<(1-\bar{s})L, \end{cases}$$

(53)

where $\bar{a} = 1/(1-\bar{s})$ and the average strain $\bar{s}$ is defined in Eq. (25). We now test the validity of the above approximation by comparison with the exact solution of Eqs. (26)–(28) under the following conditions.

Consider a sample of length $L = 9$ cm containing a hard inclusion of size $2R = 3$ cm that is centered at $Z = 4.5$ cm from the transducer. The strain values in the background regions are $s_1 = 0.17$ and $s_3 = 0.13$ but within the inclusion $s_2 = 0.03$. From Eq. (25) we find $\bar{s} = 0.11$. For simplicity, we simulated the precompression reflectivity profile $f_1(z)$ as a sine wave with a 300-μm wavelength. Because of the limited spatial resolution of the display, we can not show the 300 μm (33.3 cycles/cm) variations on the scale of the 9-cm

waveform, so we used the wavelet transform (WT) to view the effects. The WT is well suited to our purpose because it represents the *local* spatial-frequency content of the signal.

Figure 7 displays the WT calculations carried out using the commercially available software package MATLAB®. Figure 7(a) shows the WT of the precompression reflectivity profile $f_1(z)$ as well as broadband and narrow-band system response pulses $h(z)$. The ultrasonic echo signal is obtained by convolving one of the two system response functions with the reflectivity profile along the horizontal axis. Since $f_1(z)$ is the same sine wave across all three layers (there is no sonographic contrast), the WT representation of the precompression reflectivity profile is a horizontal stripe at 33.3
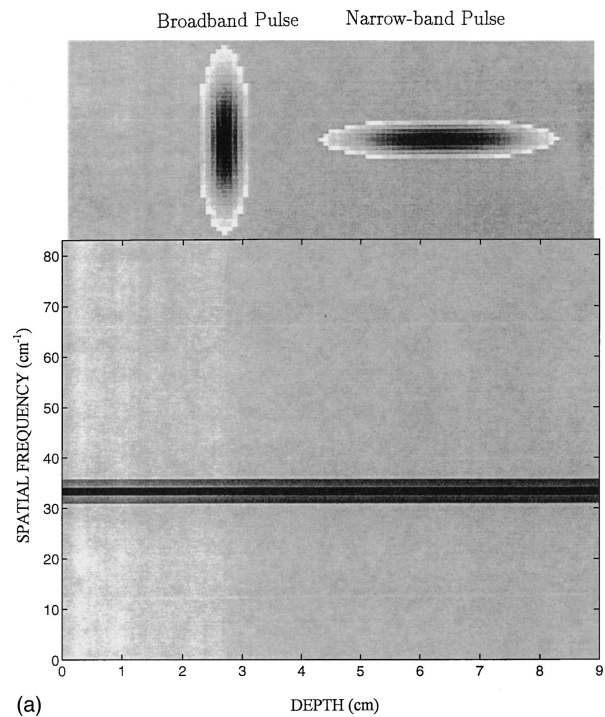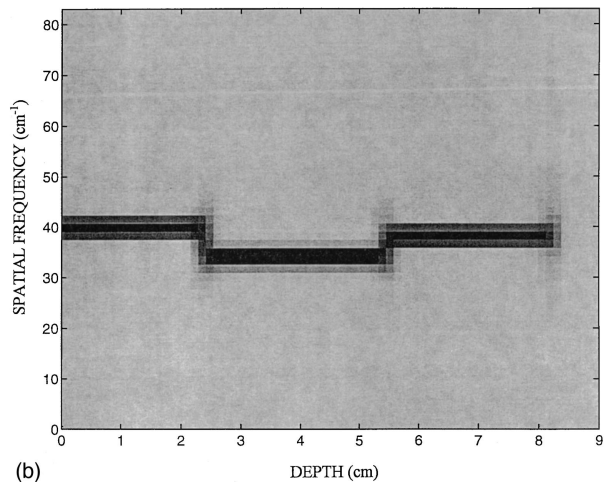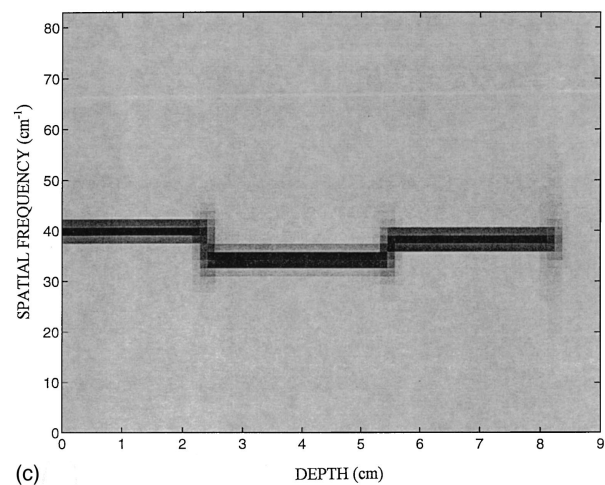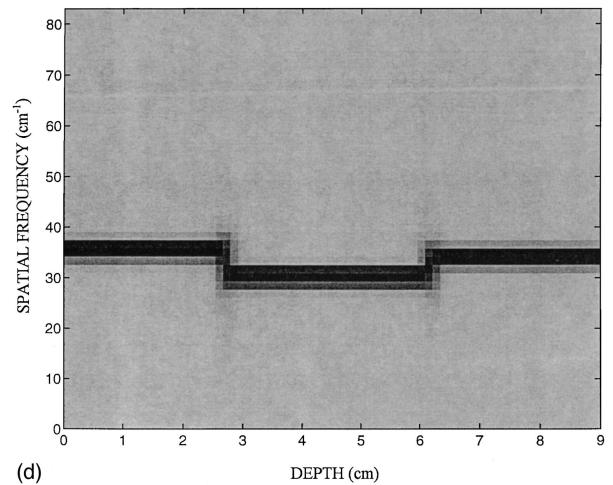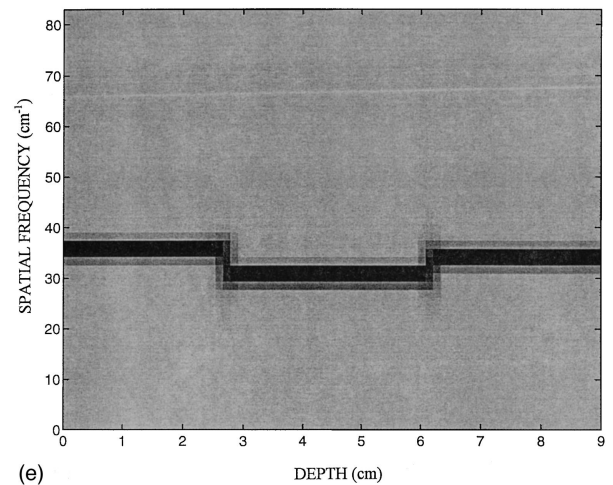
FIG. 7. Compares the precompression, postcompression, and stretched reflectivity profiles using time-frequency representation: (a) shows precompression reflectivity profile as well as broadband and narrow-band system response functions. (b) and (c) show the postcompression reflectivity profiles obtained using exact and approximate coordinate transformations. The strains in each regions are assigned as $s_1 = 0.17$, $s_2 = 0.03$, $s_3 = 0.13$. (d) and (e) are obtained by stretching the signals in (c) and (d), respectively.

cycles/cm. Note that Fig. 7(a) through (e) represents the object function and not the echo signal. Figure 7(b) and (c) display the WTs of the postcompression reflectivity profiles for the exact and approximate transformations, $f_2(z)$ and $f_{2app}(z)$, respectively. Because the strains in the three regions are different, the frequency contents of the postcompression reflectivity profiles vary. Greater deformations in the soft regions (I and III) increase the frequency of the spectral peak in those regions, i.e., $k_f' > k_f$. Since the products $k_f L_f$ and $k_f' L_f'$ are conserved, the bandwidth of a broadband reflectivity profile would increase in proportion to k_f'. The hard central region, however, is deformed very little. Consequently, the strain is small and the frequency of the spectral peak in Fig. 7(b) and (c) remains close to 33.3 cycles/cm. Strain discontinuities at the boundaries produce the broad spectral responses seen at 2.5 and 5.5 cm. The WT in Fig. 7(c), obtained from the approximation of Eq. (53), is in good agreement with Fig. 7(b), obtained from the exact formulas of Eqs. (26)–(28). This indicates that the approximation is close to the exact solution for 1-D motion, even if the strains are large.

As discussed in Sec. III A 2, we can use the average strain to improve the quality of local displacement estimates by linearly stretching the postcompression profiles. Figure 7(d) and (e) display the WTs of the exact and approximate reflectivity profiles, $f_3(z)$ and $f_{3app}(z)$, that were obtained by linearly stretching $f_2(z)$ and $f_{2app}(z)$ according to the average strain $\bar{s}=0.11$. Stretching scales down the peak frequency at all positions along z, so that the average peak frequency over L equals the precompression value of 3.33 cycles/cm. Comparing Fig. 7(d) and (e) with (a), we see that the peak frequencies in the softer regions (I and III) remain greater than the average while the peak frequency in the harder region (II) is less than the average. There is no signal decorrelation at positions along z where the local displacement equals the average displacement [$\beta(z)=0$ in Eq. (23)]. Using this property it may be possible to develop an iterative process to reconstruct the displacement profile from the pre- and postcompression signals.

IV. SUMMARY

The 2-D strain profile for a compressed medium containing an inclusion of arbitrary shape has been analyzed by studying two simpler 1-D problems: a three-layer deterministic strain profile and a one-layer stochastic strain profile. The ultrasonic scattering structure of the medium is modeled as a random continuum characterized by a Gaussian autocorrelation function. A Gaussian pulse spectrum is also assumed. Closed-form expressions for the cross-correlation functions were derived and used to design elastographic experiments for low and high input S/N conditions. The effects that correlations in the scattering structure, variations in the strain profile, cross-correlation window lengths, and the center frequency and bandwidth of the ultrasound pulse have on displacement estimates could all be determined using these expressions.

The advantages of shaping the postcompression pulse and stretching the postcompression echo signal prior to cross correlation were found to be significant. Signal stretching decreases the positional dependence of the cross-correlation function over the window length, decreasing signal decorrelation. It is also important to match the pulse spectrum to the backscatter tissue spectrum to minimize decorrelation, particularly at high S/N. Pulse shaping is a method for matching the pulse and tissue spectra. A few simple conditioning steps can greatly reduce signal decorrelation, which is a major source of uncertainty in elastographic measurements.

APPENDIX

Consider a strain profile for a sample of length L:

$$s(z)=\bar{s}+\delta s(z), \tag{A1}$$

which is written as the sum of an average component,

$$\bar{s}=\frac{1}{L}\int_0^L s(\gamma)d\gamma, \tag{A2}$$

and a fluctuating component, $\delta s(z)$. The pre- and postcompression coordinates, z and z', are related through the expression

$$z'=\int_0^z (1-s(\gamma))d\gamma. \tag{A3}$$

We first differentiate Eq. (A1) with respect to z, then invert, and finally approximate the resulting equation by

$$\frac{dz}{dz'}=(1-\bar{s})^{-1}\left(1-\frac{\delta s(z)}{1-\bar{s}}\right)^{-1}\approx\left(1+\frac{\delta s(z)}{1-\bar{s}}\right)\Bigg/(1-\bar{s}) \tag{A4}$$

for $|\delta s(z)|\ll 1-\bar{s}$ and $0\leq z\leq L$. Since $s(z)\approx s(z'/(1-\bar{s}))$, Eq. (A4) can be rewritten in integral form

$$z=\int_0^{z'/(1-\bar{s})}\left(1+\frac{\delta s(\gamma)}{1-\bar{s}}\right)d\gamma. \tag{A5}$$

[1] J. Ophir, I. Cespedes, H. Ponnekanti, Y. Yazdi, and X. Li, "Elastography: a quantitative method for imaging the elasticity of biological tissues," Ultrason. Imag. **13**, 111–134 (1991).

[2] V. P. Jackson, "Present and future role of ultrasound in breast imaging," in *Technical Aspects of Breast Imaging* (RSNA, Chicago, IL, 1994).

[3] T. J. Hall, M. F. Insana, N. M. Soller, and L. A. Harrison, "Ultrasound contrast-detail analysis: a preliminary study in human observer performance," Med. Phys. **20**, 117–127 (1993).

[4] I. Cespedes and J. Ophir, "Reduction of image noise in elastography," Ultrason. Imag. **15**, 89–102 (1993).

[5] L. S. Wilson and D. E. Robinson, "Ultrasonic measurement of small displacements and deformations of tissues," Ultrason. Imag. **4**, 71–82 (1982).

[6] R. J. Dickinson and C. R. Hill, "Measurement of soft tissue motion using correlation between A-scans," Ultrasound Med. Biol. **8**, 263–271 (1982).

[7] M. Tristam, D. C. Barbosa, D. O. Cosgrove, D. K. Nassiri, J. C. Bamber, and C. R. Hill, "Ultrasonic study of in vivo kinetic characteristics of

human tissues,'' Ultrasound Med. Biol. **12**, 927–937 (1986).

[8] T. A. Krouskop, D. R. Dougherty, and S. F. Levinson, ''A pulsed Doppler ultrasonic system for making noninvasive measurements of the mechanical properties of soft tissue,'' J. Rehabil. Res. Dev. **24**, 1–8 (1987).

[9] G. E. Trahey, S. M. Hubbard, and O. T. Von Ramm, ''Angle independent blood flow detection by frame-to-frame correlation of B-mode images,'' Ultrasonics **26**, 271–276 (1988).

[10] M. Bertrand, J. Meunier, M. Doucet, and G. Ferland, ''A model of speckle motion artifacts occurring under tissue linear transformation,'' Proc. 1989 IEEE Ultrason. Symp. 859–864 (1989).

[11] R. S. Adler, J. M. Rubin, P. H. Bland, and P. L. Carson, ''Quantitative tissue motion analysis of digitized M-mode images: gestational differences of fetal lung,'' Ultrasound Med. Biol. **16**, 561–569 (1990).

[12] P. G. M. De Jong, T. Arts, A. P. G. Hoeks, and R. S. Reneman, ''Determination of tissue motion velocity by correlation interpolation of pulsed ultrasonic echo signals,'' Ultrason. Imag. **12**, 84–98 (1990).

[13] Y. Yamakoshi, J. Sato, and T. Sato, ''Ultrasonic imaging of internal vibration of soft tissue under forced vibration,'' IEEE Trans. Ultrason. Ferro. Freq. Contr. **UFFC-17**, 45–53 (1990).

[14] M. O'Donnell, A. R. Skovoroda, B. M. Shapo, and S. Y. Emelianov, ''Internal displacement and strain imaging using ultrasonic speckle tracking,'' IEEE Trans. Ultrason. Ferro. Freq. Contr. **UFFC-41**, 314–325 (1994).

[15] F. Kallel, M. Bertrand, and J. Meunier, ''Speckle motion artifact under tissue rotation,'' IEEE Trans. Ultrason. Ferro. Freq. Contr. **UFFC-41**, 105–122 (1994).

[16] A. R. Skovoroda, S. Y. Emelianov, M. A. Lubinski, A. P. Sarvazyan, and M. O'Donnell, ''Theoretical analysis and verification of ultrasound displacement and strain imaging,'' IEEE Trans. Ultrason. Ferro. Freq. Contr. **UFFC-41**, 302–313 (1994).

[17] C. Sumi, A. Suzuki, and K. Nakayama, ''Estimation of shear modulus distribution in soft tissue from strain distribution,'' IEEE Trans. Ultrason. Ferro. Freq. Contr. **UFFC-42**, 193–202 (1995).

[18] Y. C. Fung, *A First Course in Continuum Mechanics, 2/e* (Prentice-Hall, Englewood Cliffs, NJ, 1977), Sections 7.4 and 9.7.

[19] H. Ponnekanti, J. Ophir, and I. Cespedes, ''Axial stress distributions between coaxial compressors in elastography: an analytical model,'' Ultrasound Med. Biol. **18**, 667–673 (1992).

[20] E. Konofagou, P. Dutta, J. Ophir, and I. Cespedes, ''Reduction of stress nonuniformities by apodization of compressor displacement in elastography,'' Ultrason. Imag. **17**, 50 (abstract only) (1995).

[21] A. S. Saada, *Elasticity, Theory and Applications* (Pergamon, New York, 1974).

[22] F. Dunn, P. D. Edmonds, and W. J. Fry, ''Absorption and dispersion of ultrasound in biological media,'' in *Biological Engineering*, edited by H. P. Schwan (McGraw-Hill, New York, 1969), pp. 205–332.

[23] P. M. Morse and K. U. Ingard, *Theoretical Acoustics* (McGraw-Hill, New York, 1968).

[24] A. P. Sarvazyan, ''Acoustic properties of tissues relevant to therapeutic applications,'' Br. J. Cancer **45**, 52–54 (1982).

[25] E. L. Madsen, H. J. Sathoff, and J. A. Zagzebski, ''Ultrasonic shear wave properties of soft tissues and tissuelike materials,'' J. Acoust. Soc. Am. **73**, 1346–1355 (1983).

[26] A. Macovski, *Medical Imaging Systems* (Prentice-Hall, Englewood Cliffs, NJ, 1983), Chap. 9.

[27] These assumptions are made to simplify subsequent expressions to one dimension. Nevertheless, many array systems today are focused over a relatively large field of view.

[28] F. L. Lizzi, M. Ostromogilsky, E. J. Feleppa, M. C. Rorke, and M. M. Yaremko, ''Relationship of ultrasonic spectral parameters to features of tissue microstructure,'' IEEE Trans. Ultrason. Ferro. Freq. Contr. **UFFC-34**, 319–329 (1987).

[29] M. F. Insana, R. F. Wagner, D. G. Brown, and T. J. Hall, ''Describing small-scale structure in random media using pulse-echo ultrasound,'' J. Acoust. Soc. Am. **87**, 179–192 (1990).

[30] The studies described in Refs. 28 and 29 show that the function $P(k)=k^2 \exp(-k^2 L_f^2)$ is a useful tissue model for measuring the effective scatterer size in some soft tissues. However, Eq. (9) closely approximates this model, where k_f and L_f are functions of the scatterer size and other characteristic features of the tissue microstructure.

[31] D. Middleton, *Introduction to Statistical Communication Theory* (Peninsula, Los Altos, CA, 1987).

[32] W. F. Walker and G. E. Trahey, ''A fundamental limit on the accuracy of speckle signal alignment,'' *1994 IEEE Ultrasonics Symposium* (IEEE, NY, 1994), pp. 1787–1791.

[33] The following identity is given by Middleton (Ref. 31, p. 608):

$$\int_0^\infty d\zeta \cos(\beta\zeta)\exp(-\mu^2(e^{-|\zeta|}+|\zeta|-1))=e^{\mu^2}\sum_{n=0}^\infty \frac{(-\mu^2)^n(\mu^2+n)}{n!(\beta^2+(\mu^2+n)^2)}.$$

[34] E. Weinstein and A. J. Weiss, ''Fundamental limitations in passive time-delay estimation—part II: wide-band systems,'' IEEE Trans. Acoust. Speech Signal Process. **ASSP-32**, 1064–1077 (1984).

[35] A. D. Whalen, *Detection of Signals in Noise* (Academic, New York, 1971).

[36] Changing the shape of the pulse also modifies the lateral dimensions of the resolution cell volume. To avoid decorrelation, the transducer can be apodized such that $\lambda_0 \times f$/number=constant.